Nucleation in synoptically forced cirrostratus

R.-F. Lin,[1,2] D. O. Starr,[3] J. Reichardt,[4] and P. J. DeMott[5]

[1] Formation and evolution of cirrostratus in response to weak, uniform, and constant synoptic forcing is simulated using a one-dimensional numerical model with explicit microphysics, in which the particle size distribution in each grid box is fully resolved. A series of tests of the model response to nucleation modes (homogeneous-freezing-only/heterogeneous nucleation) and heterogeneous nucleation parameters are performed. In the case studied here, nucleation is first activated in the prescribed moist layer. A continuous cloud-top nucleation zone with a depth depending on the vertical humidity gradient and one of the nucleation parameters is developed afterward. For the heterogeneous nucleation cases, intermittent nucleation zones in the mid-upper portion of the cloud form where the relative humidity is on the rise because existent ice crystals falling from higher nucleation zones do not efficiently deplete the excess water vapor and ice nuclei are available. Vertical resolution as fine as 1 m is required for realistic simulation of the homogeneous-freezing-only scenario, while the model resolution requirement is more relaxed in the cases where heterogeneous nucleation dominates. Bulk microphysical and optical properties are evaluated and compared. Ice particle number flux divergence, which is due to the vertical gradient of the gravity-induced particle sedimentation, is constantly and rapidly changing the local ice number concentration, even in the nucleation zone. When the depth of the nucleation zone is shallow, particle number concentration decreases rapidly as ice particles grow and sediment away from the nucleation zone. When the depth of the nucleation zone is large, a region of high ice number concentration can be sustained. The depth of nucleation zone is an important parameter to be considered in parametric treatments of ice cloud generation.

1. Introduction

[2] The optical depth of cirrus, one of the controlling factors determining its associated net cloud radiative forcing, depends on the cloud ice water path (IWP) and effective particle size [e.g., *Foot*, 1988]. Some state-of-the-art general circulation models (GCMs) now predict hydrometeor mixing ratios [e.g., *Del Genio et al.*, 1996; *Fowler et al.*, 1996]. However, realistic prediction of cirrus optical and microphysical properties requires accurate estimation of the number concentration of ice particles generated in the nucleation regime. Using an approximate analytical solution validated by parcel model simulations, *Kärcher and Lohmann* [2002] developed a parameterization scheme for ice particle number concentration via homogeneous freezing nucleation of aerosol particles and implemented it into the European Center Hamburg (ECHAM) GCM [*Lohmann and Kärcher*, 2002] to examine the aerosol effects on the ice cloud and Earth-atmosphere radiative budgets. Despite advances in parameterization schemes of aerosol effects on ice initiation, our fundamental understanding of the evolution of synoptically forced cirrus still lags. Studies based on parcel models are typically not able to provide information about the entire cloud from cloud base to cloud top. Moreover, parcel model studies usually assume that the ice particles are lifted with the parcel (no particle fallout or fall-in) and that there is no exchange of mass or heat with the environment. Neglect of particle fallout/fall-in is questionable for weak forcing conditions, where nucleation may last several to more than 10 min. Thus a model of one-dimension (1-D) or higher [e.g., *Jensen et al.*, 1994a, 1994b; *Khvorostyanov et al.*, 2001; *Sassen et al.*, 2002] is needed to adequately estimate cloud bulk properties over the entire cloud depth. In our study a 1-D model with an explicit microphysical scheme is used to simulate a column of air lifted by a gentle updraft.

[1]Goddard Earth Sciences and Technology Center, University of Maryland Baltimore County, Baltimore, Maryland, USA.
[2]Also at Laboratory for Atmospheres, NASA Goddard Space Flight Center, Greenbelt, Maryland, USA.
[3]Laboratory for Atmospheres, NASA Goddard Space Flight Center, Greenbelt, Maryland, USA.
[4]DWD-Meteorologisches Observatorium Lindenberg, Tauche, Germany.
[5]Department of Atmospheric Science, Colorado State University, Fort Collins, Colorado, USA.
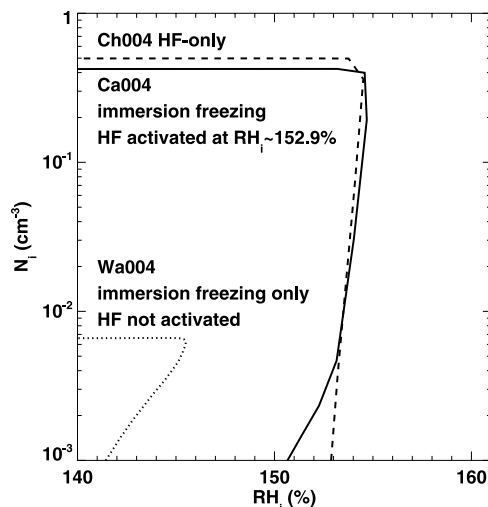
Figure 1. Ice particle number concentration N_i in an ascending parcel (4 cm s^{-1}) as a function of the parcel RH$_i$. Curves Wa004 and Ca004 (both HF and immersion freezing modes are allowed) are from parcel simulations using DeMott's model with starting temperatures −40°C and −60°C, respectively (see *Lin et al.* [2002a] for details). For reference, the result of Ch004 (HF only) is also plotted.

[3] For synoptically forced cold cirrus, in which the vertical wind speed is less than 0.1 m s^{-1} and the temperature is less than −40°C, homogeneous freezing nucleation (HF) of aqueous solution particles and heterogeneous nucleation (HET) via deposition nucleation and/or immersion and contact freezing of aqueous solution particles can be activated. Ice nuclei (IN) activated at a threshold relative humidity with respect to ice (RH$_i$) greater than that for HF are generally not of meteorological interest. Therefore unless an air parcel is devoid of ice nuclei, it is expected that as the air parcel ascends and cools, heterogeneous nucleation will be activated first. Depending on the magnitude and duration of forcing and the number concentration of activated IN, HF may be partially or completely suppressed [*Lin et al.*, 2002a]. For synoptically forced cirrus, heterogeneous nucleation may be the dominant nucleation mode and the predicted ice crystal number concentration N_i may be significantly reduced in comparison to a cloud formed via the HF process in the presence of heterogeneous IN [*Heymsfield and Miloshevich*, 1995; *DeMott et al.*, 1997].

[4] From the governing equations to predict the amount of ice particles being generated, the particle number concentration is determined by the activation RH$_i$ and ice particle formation rate of the mode $\dot{N}_i$, given the forcing and temperature. Testing a fair range of these two controlling factors provides useful insight into the system because the detailed formulation for heterogeneous nucleation modes is not understood well.

[5] In this study, HF of sulfuric acid haze particles is explicitly formulated by adopting the effective freezing temperature scheme [*Sassen and Dodd*, 1988; *Heymsfield and Miloshevich*, 1993]. This scheme predicts ice nucleation in close agreement with water activity based on homogeneous nucleation theory [*Koop et al.*, 2000]. For

the formulation of heterogeneous nucleation (HET), we used the exponential form

$$N_{IN} = N_0 \exp[\beta(S_i - S_i^*)], \qquad (1)$$

where N_{IN} indicates the number concentration of activated IN; N_0 is a small number equal to 10^3 m^{-3}; S_i and S_i^* are ice supersaturation ratio and activation ice supersaturation ratio, respectively; and β controls the IN activation rate above S_i^*. Parameters β and S_i^* (hereafter, heterogeneous nucleation parameters) may be functions of IN and aerosol species, temperature, and updraft speed. This formula is the general form of the parameterization scheme for deposition/condensation freezing nucleation of *Meyers et al.* [1992, hereinafter referred to as M92]. Parcel simulations of immersion freezing in sulfuric acid haze particles by DeMott (results can be found in the work of *Lin et al.* [2002a]) indicate that the exponential form may be used to approximate the exact formulations for the heterogeneous and homogeneous freezing, as demonstrated in Figure 1, where results from parcel model simulations using exact formulations yield a linear relationship between logarithm N_i and RH$_i$. In the parcel model simulations presented here, $N_i = N_{IN}$ before HF is activated. This approximation (equation (1)) is easy to implement in any model; however, it does have a weakness. For homogeneous freezing nucleation, nucleation does not cease at the peak RH$_i$. Thus this approximation could underestimate the predicted ice particle number concentration by homogeneous freezing if it is not carefully implemented. Furthermore, the exponential form treats IN as if there is unlimited number of IN. An easy way to improve this is to add an upper bound of S_i to the equation, as many have done [e.g., *Meyers et al.*, 1992; *Khvorostyanov et al.*, 2001].

[6] For the nucleation studies reported here, we tune our simulations to reproduce the gross features of a long-lived cirrostratus event that was observed by the GKSS Raman lidar [*Reichardt et al.*, 1996] above the Esrange research facility (67.9°N, 21.1°E) near Kiruna, Sweden, on 16–17 January 1997. A reasonable match was achieved using an imposed "synoptic" vertical motion and initial relative humidity profile. Many structural features of this observed cloud are quite similar to those seen in other studies of synoptic cirrus systems in the midlatitude, such as reported by *Sassen et al.* [1989], *Starr and Wylie* [1990], *Sassen et al.* [1990], and many others since. We do not delve into the possibly important effects of mesoscale forcing which may be a significant factor in this case but rather focus on the nucleation processes operating in a simplified framework. In the following, the 1-D model is first briefly described in section 2, followed by a summary of the lidar measurement and initial conditions in section 3. The HF scenario is discussed in section 4 with an emphasis on the effects of model resolution. The results of HET simulation series are presented in section 5 followed by concluding remarks (section 6).

2. One-Dimensional Cirrus Model With Explicit Microphysics

[7] The cirrus model is the 1-D time-dependent version of a cirrus model developed to simulate tropical cirrus anvil

outflow [*Lin*, 1997]. Ice crystals and H_2SO_4 aerosol particles are grouped into bins according to their ice mass and solute mass, respectively, to resolve the evolution of particle size distributions (PSDs). For a given bin k in any grid box, the mean H_2O mass (m_k) and number concentration (N_k) are both predicted. The bin boundaries (x_k) follow $x_{k+1}/x_k = c$, where c is about 1.5 and 2.2, and x_1 is about 3×10^{-15} and 10^{-21} kg for ice crystals and aerosols, respectively. The nucleation temperature of ice crystals is also tracked. Any given ice bin is further divided into sub-bins according to the nucleation temperature for further analysis. When two ice crystals collide and form an aggregate, the nucleation temperature of the larger particle is assigned to the aggregate. For simplicity, ice crystals in all simulations are assumed to be columnar, as *Bailey and Hallett* [2004] concluded that from diffusion chamber experiments, ice crystals are mostly polycrystals with columnar characteristics and columns for $T < -40°C$ and $RH_i > 110\%$. We use a power-law relationship between crystal length and mass [*Auer and Veal*, 1970; *Heymsfield*, 1972; *Mitchell and Arnott*, 1994]. The corresponding aspect ratio relationship follows $d = 0.7L$ for $L < 100$ μm and $d = 6.96L^{1/2}$ for $L > 100$ μm, where the symbols d and L are the width and length of ice crystals in microns, respectively.

[8] The governing equation for particle concentration in the kth size bin, N_k, is as follows:

$$\frac{\partial N_k}{\partial t} = -\frac{\partial}{\partial z}(W - V_{t,k})N_k + W\frac{d\ln\rho}{dz}N_k + \left.\frac{\partial N_k}{\partial t}\right|_{\text{growth}} + \left.\frac{\partial N_k}{\partial t}\right|_{\text{agg}}$$
$$+ \left.\frac{\partial N_k}{\partial t}\right|_{\text{HF}} + \left.\frac{\partial N_k}{\partial t}\right|_{\text{HET}}, \quad (2)$$

where the first and the second right-hand side (RHS) terms are the particle flux divergence in the vertical direction and a compensating term due to anelastic approximation, respectively. The other RHS terms, from left to right, are local tendencies due to particle growth, aggregation, homogeneous freezing, and heterogeneous nucleation. W is the vertical air velocity, and V_t is the ice crystal terminal fall speed. Ice crystals initiated via heterogeneous nucleation (HET) always start from the first size bin (about 1 μm). HF-produced ice crystals may start from other bins consistent with the mass of H_2O in the freezing aerosol; thus this setup is useful for freezing of large aerosols or activated droplets at warmer temperatures ($T > -45°C$). Note that at $-40°C$, H_2SO_4 solution particles with solute mass 10^{-14} and 10^{-12} g are activated at radii equal to 1.10 and 11.0 μm, respectively. Ice particle fall speed, a function of particle size, is calculated using *Böhm* [1989]. Model sensitivity to terminal fall velocity of ice crystals is briefly examined at the end of section 5. A second-order in time and second-order in space monotonic upstream-biased transport scheme [*Allen et al.*, 1991] is used to treat the particle transport in the vertical direction.

[9] Time splitting is applied to treat the imposed rate of uplift and local particle growth separately. The time step is 5 s for the advection terms when the grid spacing $\Delta z \geq 4$ m and is reduced for a smaller grid spacing, while the time step is always 0.1 s for particle growth. First, the local tendencies of moisture and heat (represented by the tendency of potential temperature in the 1-D model) due to vertical

advection are calculated, as is the advective tendency of particle concentration on a bin-by-bin basis accounting for fall speed. Then, the particle growth in each grid volume is treated in a Lagrangian fashion where the water vapor mixing ratio and potential temperature are changing with time due to the advection tendencies and phase change (depositional growth). The imposed advective tendencies of heat and moisture are held constant over the advective time interval, and the particle concentration is held fixed at the value predicted for the end of the advective time interval.

[10] A hybrid method-of-moment scheme is adopted to treat the terms

$$\left.\frac{\partial N_k}{\partial t}\right|_{\text{growth}}$$

and

$$\left.\frac{\partial N_k}{\partial t}\right|_{\text{agg}}$$

in equation (2) [*Rokicki and Young*, 1978; *Ochs and Yao*, 1978; *Chen and Lamb*, 1994]. It is assumed that the particle size distribution (PSD) inside a bin is a piecewise-linear function. Instead of integrating the growth and collection equations over the PSD inside a given bin, the mean mass of a given bin is used to estimate the mean growth rate and interaction with other bins through collection. The piecewise-linear function is then used to estimate mass and number of particles transported (via growth or decay and aggregation) to other bins. This scheme has been demonstrated to produce fairly good simulations of the evolution of PSDs [*Chen and Lamb*, 1994] and is more flexible than strict method-of-moment schemes [e.g., *Tzivion et al.*, 1987]. Aggregation is included in the simulations reported here (aggregation coefficient of 0.1) but there is little sensitivity due to the small number concentrations of ice crystals here, even in the cloud top zone with greater concentrations of smaller crystals (sensitivity tests were performed with aggregation coefficients ranging from 0 to 1).

[11] The diffusional growth rate of ice crystals is calculated using electrostatic analogy and prolate approximation for the capacitance of columnar ice crystals [*Pruppacher and Klett*, 1997]

$$\frac{dm_k}{dt} = \frac{4\pi C_k S_i}{\dfrac{R_v T}{D'e_i} + \dfrac{L_s}{K'T}\left(\dfrac{L_s}{R_v T} - 1\right)}. \quad (3)$$

In this study the deposition coefficient is set to 1.0 because existent data suggest that the coefficient decreases with increasing temperature [*Pruppacher and Klett*, 1997, Table 5.5; *Haynes et al.*, 1992; *Heymsfield and Miloshevich*, 1998] and the predicted N_i is not very sensitive to the coefficient when its value is between 0.24 and unity [*Lin et al.*, 2002a; *Gierens et al.*, 2003; *Haag et al.*, 2003a]. Radiation effects on ice crystal growth are ignored. *Stephens* [1983] estimated that at P = 200 mb and T = $-56.6°C$, the effective relative humidity changes due to direct radiation impact for columnar particles of several hundred microns in length are about 10% for the maximum cooling case and

Table 1. Simulation Identifiers[a]

Nucleation Mode	Run ID	$S_i^* \times 100$	β
	M92	~5	~13
HET	S20β40	20	40
	S30β40	30	40
	S20β60	20	60
	S30β60	30	60
HF		~59.5[b]	~112[b]

[a]M92 adopts coefficients from *Meyers et al.* [1992].
[b]For quick comparison purposes only. These values are derived for the parcel released at z = 8.822 km. See section 4 for details.

−15% for the maximum warming case, corresponding to the top and base, respectively, of an optically thick cloud. The effective relative humidity change inside this simulated cirrostratus would be smaller than those extreme numbers because (1) the cloud is not optically thick or (2) the temperature of the ground is cold. Furthermore, the simulated cloud is highly ice-supersaturated, as indicated in sections 4 and 5. We thus expect the direct impact of radiation is secondary compared with the uncertain forcing term. The diffusional growth of aerosol is also explicitly calculated.

[12] Homogeneous freezing of H_2SO_4 aerosols is computed using the effective freezing temperature approximation [*Sassen and Dodd*, 1988], ($T_{eff} = T + \lambda\Delta T_m$, where T_{eff} and ΔT_m are effective freezing temperature and melting point depression, respectively, and $\lambda = 2$) together with a fitted HF formula for pure water [*Heymsfield and Miloshevich*, 1993]. The aerosol is assumed to be lognormally distributed with N_a = 200 cm^{-3}, pure H_2SO_4 mode radius of 0.02 μm, and a distribution width of 2.3. The number concentration of freezing aerosols is not sensitive to the initial haze PSD when the ascent is weak [*Jensen et al.*, 1994b; *Kärcher and Lohmann*, 2002; *Lin et al.*, 2002b]. Note that although we do not use equation (1) to calculate homogeneous freezing, we will use the associated effective β and S_i^* for HF (Table 1) for qualitative discussion.

[13] Heterogeneous nucleation in the upper troposphere is still a subject of active research. *Haag et al.* [2003b] has concluded from the interpretation of aircraft measurements during the Interhemispheric Differences in Cirrus Properties from Anthropogenic Emissions (INCA) that heterogeneous nucleation as well as homogeneous nucleation plays a role in the formation of cirrus in the polluted regions of the Northern Hemisphere. The discrepancy between the laboratory measured RH$_i$ to activate homogeneous freezing and the highest observed upper-tropospheric RH$_i$ implies that heterogeneous nucleation might be the dominant nucleation mode when the forcing is weak [*Heymsfield and Miloshevich*, 1995]. Table 1 shows the tested values of β and S_i^* in this study. Although the derived β and S_i^* in M92 were for temperatures between −7°C and −20°C and S_i between 0.02 and 0.25, they are adopted to the temperature and S_i ranges considered here and are expected to represent the most favorable condition for heterogeneous nucleation. A reasonable expectation is that the physically appropriate values of β and S_i^* lie between M92 and homogeneous nucleation values. The tested values of β loosely follow those inferred from DeMott's

parcel study of immersion freezing nucleation: $\beta \sim 47$ and 60 for the −40°C and −60°C cases, respectively (Figure 1).

[14] Tracking IN by implementing a binned IN category is intuitively straightforward but expensive in terms of storage space [*Khain et al.*, 2000]. We adopt the IN tracking approach in this study. The number concentration of IN that are activated from $S_{i,k}$ to $S_{i,k+1}$, IN$_k$, is calculated according to (1). We do not impose an upper bound of S_i to equation (1) for any of our M92 or HET simulations. The IN bin boundaries follow $S_{i,k} - S_{i,k-1} = 0.01$ for $S_{i,k} \leq 0.25$; and $S_{i,k} - S_{i,k-1} = 0.005$ for $S_{i,k} > 0.25$. The model treats advection of IN$_k$ by the vertical wind explicitly. New ice particles are formed by HET when $S_i > S_{i,k+1}$ and IN$_k$ are available, i.e., IN$_k$ are not depleted due to prior nucleation. Thus considering a volume of air, once $S_i > S_{i,k+1}$, all of the IN in bin k nucleate and IN$_k$ becomes zero. Larger values of S_i ($S_i > S_{i,k+2}$) must be subsequently achieved for further nucleation to occur. Alternative approaches are tested and discussed in section 5.

3. Simulation Setup

[15] The numerical simulations of the long-lived cirrostratus near Kiruna, Sweden, on 16–17 January 1997 serve two purposes. First, we examined nucleation processes in the context of an observed synoptically forced cirrus cloud (this paper). Second, we provided detailed microphysical data for calculations of cirrus optical properties (*Reichardt et al.* [2002b]; a more detailed paper is in preparation). The lidar observations are shown in Figure 2. The cirrus cloud system is associated with a strong northwesterly jet stream (75 m s^{-1}) and surface warm front located over central Sweden. The cloud started to develop between 8.6 and 9.0 km at around 2010 UTC of 16 January 1997. As the cloud evolved, many embedded structures were present in the nonuniform and sometimes layered cloud field. In general, the cloud appeared to be more cellular near the cloud top, possibly corresponding to a generation zone, with elongated patterns, resembling mesoscale fall streaks
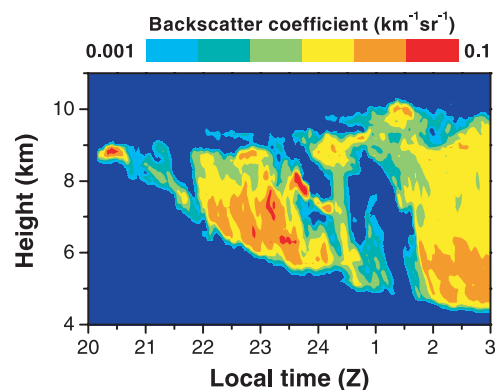
Figure 2. Height versus time display of backscatter coefficient generated from consecutive lidar profiles of the cirrus cloud measured on 16–17 January 1997 over northern Sweden. For experimental details, see *Reichardt et al.* [2002a].
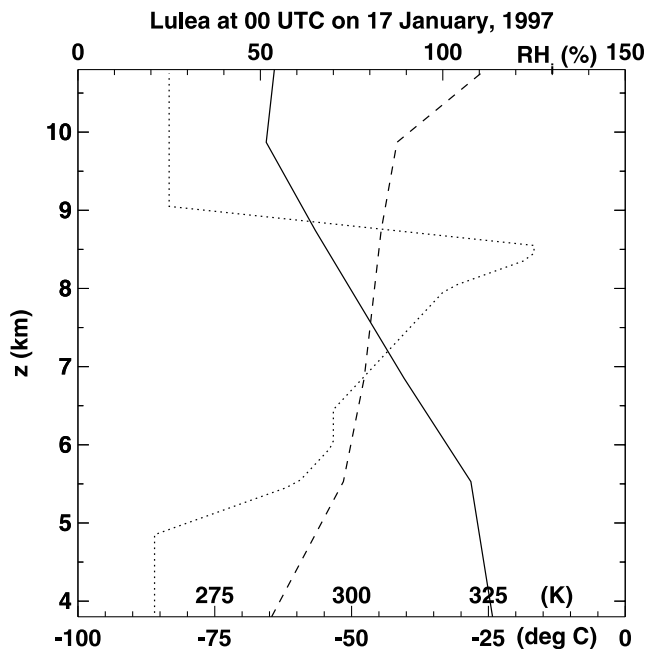
Figure 3. Radiosonde data (temperature is indicated by the solid curve and potential temperature is denoted by the dash curve) taken at Luleå at 00 UTC on 17 January 1997. The RH_i profile, which is denoted by the dotted curve, is selected after several sensitivity tests.

[*Sassen et al.*, 1989], that sometimes extended from mid-cloud to cloud base. In the work presented here, we do not attempt to explicitly model the small-scale cloud structure but focus on the general cloud development (the overall cloud top and base heights) and the 30-min averaged cloud extinction-coefficient profiles from three time periods, which are assumed to respond to the synoptic forcing and used to constrain the values of uncertain parameters. A description of the prototype to constraining the model and comparisons between observation and simulation are given by *Reichardt et al.* [2002b].

[16] Local soundings of atmospheric parameters were not available for that day. Instead, temperature and pressure profiles (Figure 3) based on the 0000 UTC radiosonde from Luleå, Sweden (65.6°N, 22.1°E) are used as model input. Luleå is approximately 265 km downwind of Kiruna. The Luleå humidity profile is used as a first guess and, as a tunable parameter, subsequently adjusted in sensitivity tests. The other tunable parameter is the synoptic scale rate of uplift W, which is assumed to be constant with respect to time and height in the model domain (3.8 to 10.8 km). A considerable number of simulations were performed to obtain a reasonable humidity profile (Figure 3) and the corresponding W (5 cm s^{-1}) that could reproduce the overall characteristics of the observations. The time-averaged extinction coefficient profiles for those given time periods of simulation M92 resemble qualitatively those measured from the lidar [*Reichardt et al.*, 2002b]. From simulations of W = 3, 5, 7 cm s^{-1}, together with several different initial humidity profiles, the conclusion can be drawn that the latter affects primarily the development of the cloud in the first 3 hours, while the evolution of cloud height, cloud

depth, and IWP throughout the 7-hour simulations depends mostly on W.

4. Homogeneous Freezing (HF) Scenario

[17] For an ascending parcel that is devoid of IN and lifted by a constant speed updraft, homogeneous nucleation may continue for 10–30 m of vertical displacement once it is activated [*Lin et al.*, 2002a]. Is it necessary to have a model vertical grid size of 20 m or smaller to simulate homogeneous nucleation explicitly? To answer this question, vertical grid spacings of 100, 20, 4, 2, and 1 m are tested. The differences between the simulations are dramatic (Figure 4). The 100-m and 20-m simulations exhibit a series of nucleation pulses at cloud top, encircled by the white curves in the lower left and center panels of Figure 4, which lead to formation of periodic fall streaks. In contrast, only a single major fall streak forms in the 4-m, 2-m (not shown), and 1-m runs. These results demonstrate a strong sensitivity to vertical grid resolution and suggest that very fine resolution is required to realistically treat the HF process.

[18] *Sassen and Dodd* [1989] and *Khvorostyanov et al.* [2001] have described similar appearing pulsation in their models as cycles of nucleation, crystal growth and decreasing moisture (RH_i), particle fallout, continued adiabatic cooling and increasing RH_i, and reinitiation of nucleation. As in the work of *Sassen and Dodd* [1989], the forcing here is constant and continuous. Conceptually, we can view the air column as a vertical stack of air parcels of small but finite sizes where these parcels are lifted by the mean wind W. In the absence of vertical mixing, ice particles may only enter from the overlying parcel and may only exit into the parcel beneath via the fall out processes. Once nucleation becomes active and ice crystals start to form in parcel j, there is no mechanism for the particles to travel to the overlying parcel $j + 1$ ($z(j) < z(j + 1)$; z varies with time). As a consequence, particles in parcel j cannot affect the RH_i evolution in parcel $j + 1$. If parcel j is the uppermost parcel containing ice and RH_i decreases with height above $z(j)$, then continued forcing (lifting) will cause rising RH_i in parcel $j + 1$ and ultimately nucleation in that parcel. At fine resolution, this becomes a continuous nucleation process at cloud top. In a Eulerian model with vertical motion forcing, once crystals are present in a grid volume, vertical advection will quickly transport some to the overlying grid volume where they will be regarded, numerically, as dispersed throughout that volume. There, they grow by diffusion if RH_i is favorable, reducing RH_i (or the rate of RH_i increase) and consequently delaying or suppressing the onset of nucleation within that grid volume. We conclude that the pulsating nucleation process in the 20-m and 100-m runs is nonphysical, an artifact of inadequately resolving the cloud-top nucleation zone.

[19] Considering the 4-m, 2-m, and 1-m simulations, two distinct regions are evident in the time-height displays of IWC (ice water content) and N_i (Figure 4). The fall streak region develops in response to the initial nucleation episode between simulation times 1 and 1.5 hours (Figure 4f) in highly supersaturated air over about a 200-m depth and progressively extends downward as ice crystals sediment. The fall streak zone is moderately supersaturated (115% > RH_i > 100%) after simulation time t = 4 hours except for the
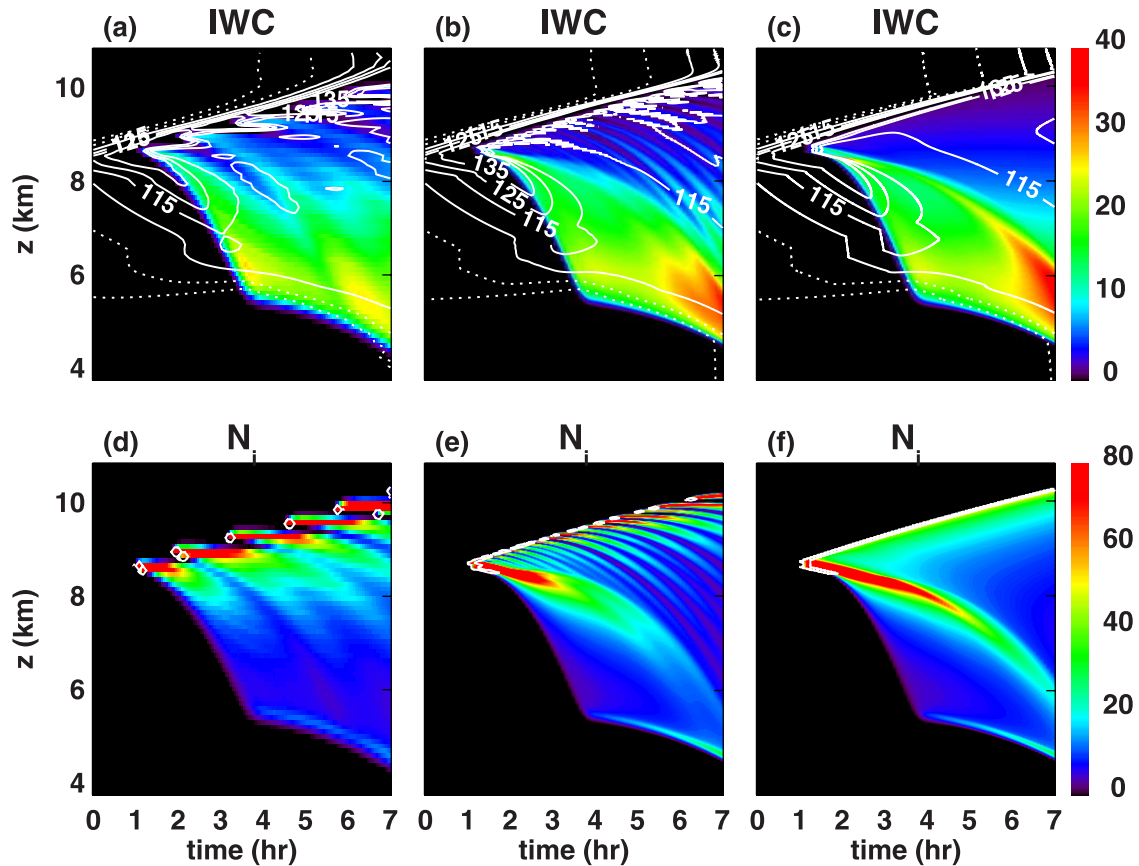
Figure 4. Effect of vertical grid spacing on the simulated IWC (mg m^{-3}) and N_i (liter^{-1}) for the HF scenario. From left to right, $\Delta z = 100$, 20, and 1 m, respectively. (a–c) The white curves indicate RH$_i$ (dotted: 60 and 80%, solid: 100, 115, 125, 135%), while (d–f) the white curves outline the nucleation zones.
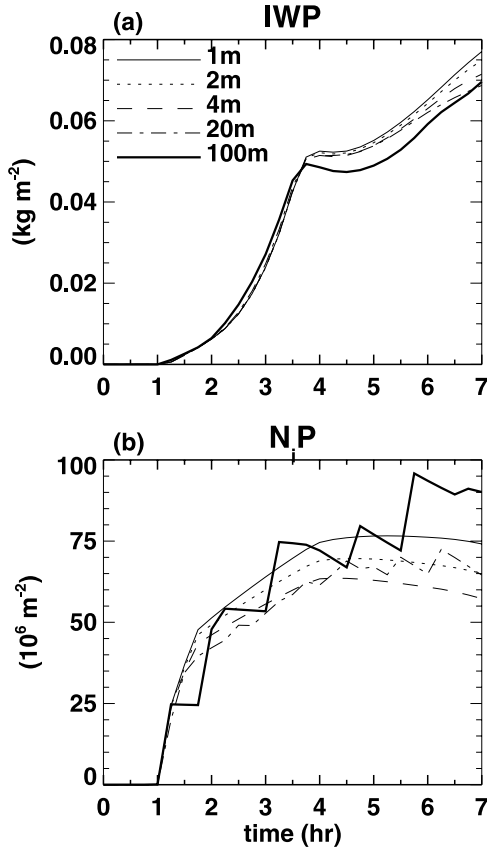
cloud base sublimating zone. Note that the fall streak contains most of the ice mass in the column, reflecting the crystal growth that occurs as the particles fall through the supersaturated layer. We call the cloudy region above the fall streak region as the cloud top region, in which IWC is small, supersaturation is large, and N_i increases with altitude. The cloud top region is formed by ice crystals generated in the continuous cloud-top nucleation zone, outlined by the white lines in Figure 4f.

[20] Cloud-top height increases with a speed slightly faster than the mean vertical wind speed because the grid boxes above the moist layer achieve HF nucleation threshold sequentially as the entire air column ascends (through the grid) and adiabatically cools. The rate at which cloud height increases is determined by W, T, P, nucleation threshold, and particularly the initial vertical gradient of RH$_i$ above the moist layer.

[21] Time series of simulated IWP and the column integrated N_i (N_i path, hereafter, N_iP) are compared in Figure 5. It is evident that the 100-m run underestimates IWP and that the nucleation pulses in the 100-m and 20-m runs result in significant oscillations of N_iP. Furthermore, the IWP of the 4-m, 2-m, and 1-m runs are quite close but begin to diverge over the last 2 hours, while the N_iP of the 4-m and 2-m simulations are significantly smaller than in the 1-m run. An increase in grid spacing from 1-m to 4-m

results in a slight suppression of the peak RH$_i$ (as small as 0.2% between the 4-m, 2-m, and 1-m runs, Figure 6a) but a large decrease in the particle formation rate $\dot{N}_i$ (Figure 6b). This is a consequence of the extreme sensitivity of the homogeneous freezing mechanism to RH$_i$. The profiles of N_i for the simulations and the number concentration of freezing haze particle, $N_{a,frz}$, for the 1-m simulation are shown in Figure 6c. Note that $N_{a,frz} = N_i$ for a parcel simulation, whereas such a relationship does not exist between $N_{a,frz}$ and N_i in a 1-D simulation. The peak N_i is much smaller than its corresponding $N_{a,frz}$, indicating that particle divergence is already very active in the nucleation zone, i.e., the reduced value of N_i in the 1-D simulation reflects net loss due to particle fallout. The effects of particle fall speed are very evident in the N_i profiles, e.g., values of N_i at 40 m below the nucleation zone are nearly half as large as in the nucleation zone itself in the 1-m simulation. To further illustrate this process, consider that the particle residence time, defined as $\Delta z/V_t$, for 10, 20, and 100 μm crystals, is about 6, 1.6, and 0.1 min, respectively, in the 1-m simulation.

[22] The significant differences between the 1-m and the 2-m simulations prompt the question of whether the grid spacing has to be reduced still further. To verify the 1-m result, an independent parcel simulation using the same microphysical module is done for the parcel with an initial

(a) IWP

(b) N$_i$P

Figure 5. Effect of vertical grid spacing on IWP and N$_i$P.

the influx from the top. Therefore the assumption that ice crystals generated in an air parcel would stay together for a considerable time does not apply to synoptically forced cirrostratus. As a result of the particle flux divergence, the water vapor uptake (per air volume) is reduced. The change of S_i with respect to time quantifies this efficiency. Following *Kärcher and Lohmann* [2002],
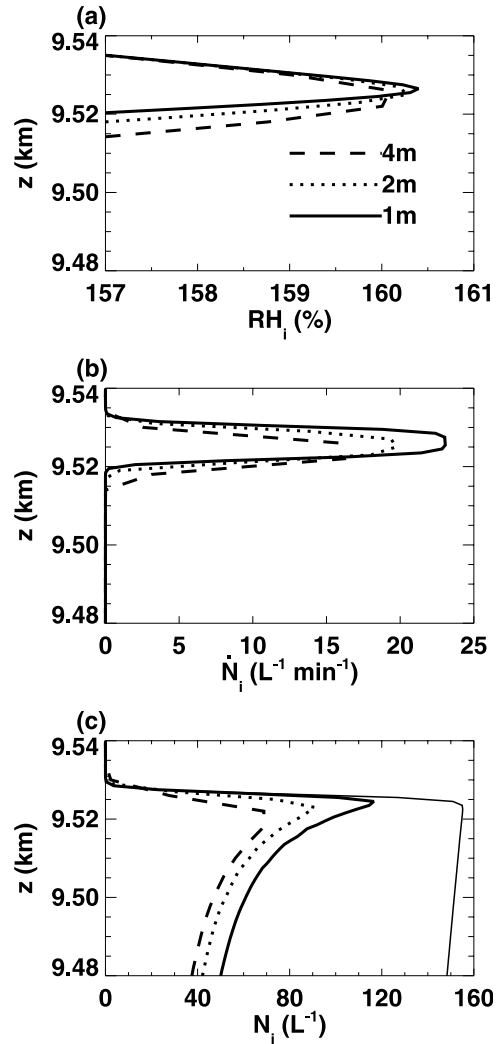
$$\frac{dS_i}{dt} = a_1 W(S_i + 1) + [a_2 + a_3(S_i + 1)]\frac{dq}{dt}, \qquad (4)$$

where

$$a_1 = \frac{g}{T}\left(\frac{L_s}{R_v C_p T} - \frac{1}{R_d}\right),$$

$$a_2 = \frac{1}{q_s},$$

$$a_3 = \frac{\rho \varepsilon L_s^2}{C_p P T},$$

Figure 6. Effect of vertical grid spacing on the cloud-top nucleation zone of the HF scenario at simulation time $t =$ 235 min. Note the thin solid curve in Figure 6c is the number concentration of freezing haze particles from the 1-m simulation.

altitude of 8.8215 km. If subject to the same lift as in the 1-D simulations, this parcel would reach 9.5265 km at time 235 min, the altitude of peak RH$_i$ in Figure 6. The simulated air parcel reaches its peak RH$_i$ of 160.35% at height 9.525 km, when N_i is about 80 L^{-1}. At time 235 min (30 s later), N_i is about 130 L^{-1} and RH$_i$ becomes 160.22%. Shortly thereafter, nucleation ends, and N_i is about 160 L^{-1}, which is much greater than the corresponding N_i of the 1-m simulation but is reasonably close to 150 L^{-1} of freezing haze particles at the associated height.

[23] To further understand the cloud top nucleation zone and the cloud top region, we consider trajectories through our 1-D grid. Trajectory A (Table 2) represents air that goes through the cloud-top nucleation zone in the 1-m simulation. A parcel following trajectory A enters the nucleation zone from above as the cloud top is ascending faster than the vertical air speed. Shown in Figure 7 are the time-dependent RH$_i$-100, N_i, and the ice crystal formation rate $\dot{N}_i$ interpolated along the trajectory. In the same figure the corresponding PSDs are shown for the given time (or height) without any interpolation. Along trajectory A, nucleation is active for about 8 min (see inset in Figure 7a). Although the peak N_i is more than 100 L^{-1}, N_i decreases rapidly afterward, while the PSD narrows and the mean size of the remaining crystals grows in response to diffusional growth (Figure 7b). The decrease in N_i manifests the particle flux divergence caused by the outgoing flux (downward positive) from the bottom exceeding

Table 2. Trajectories A and B

| Parcel ID	z_0	Nucleation Starting	
		Time, min	Height, km
A	8.663	126	9.041
B	8.2	95	8.485

and $(dq)/(dt)$ is the change of water vapor mixing ratio with time. Consequently, when

$$-\frac{dq}{dt} < \frac{a_1 W(S_i + 1)}{[a_2 + a_3(S_i + 1)]},$$

ice particles at a given location do not uptake excess water vapor efficiently $((dS_i)/(dt) > 0)$, and vice versa. *Khvorostyanov and Sassen* [1998] have defined the phase relaxation time as the e-folding time required to remove the mass of excess water vapor, $q - q_s$. This phase relaxation time does not necessarily correspond to the supersaturation ratio relaxation time constant. For example, a parcel may have a finite phase relaxation time, while the supersaturation ratio is actually increasing. To further demonstrate this point, the RH_i change rate (dRH_i/dt) is calculated and plotted using model output of $(dq)/(dt)$, S_i, T, and P. As shown in Figure 7a, dRH_i/dt becomes positive after $t = 4.5$ hours and is about 2% per hour at the end of simulation.

[24] Still considering the 1-m resolution simulation, how is a layer of large N_i sustained for such a long time at the top of the fall streak, although its peak value is decreasing with time? Trajectory B represents air that as it ascends, encounters the fall streak descending from above. Recall that similar to the cloud top nucleation zone, there is a cloud base nucleation zone that persists until it
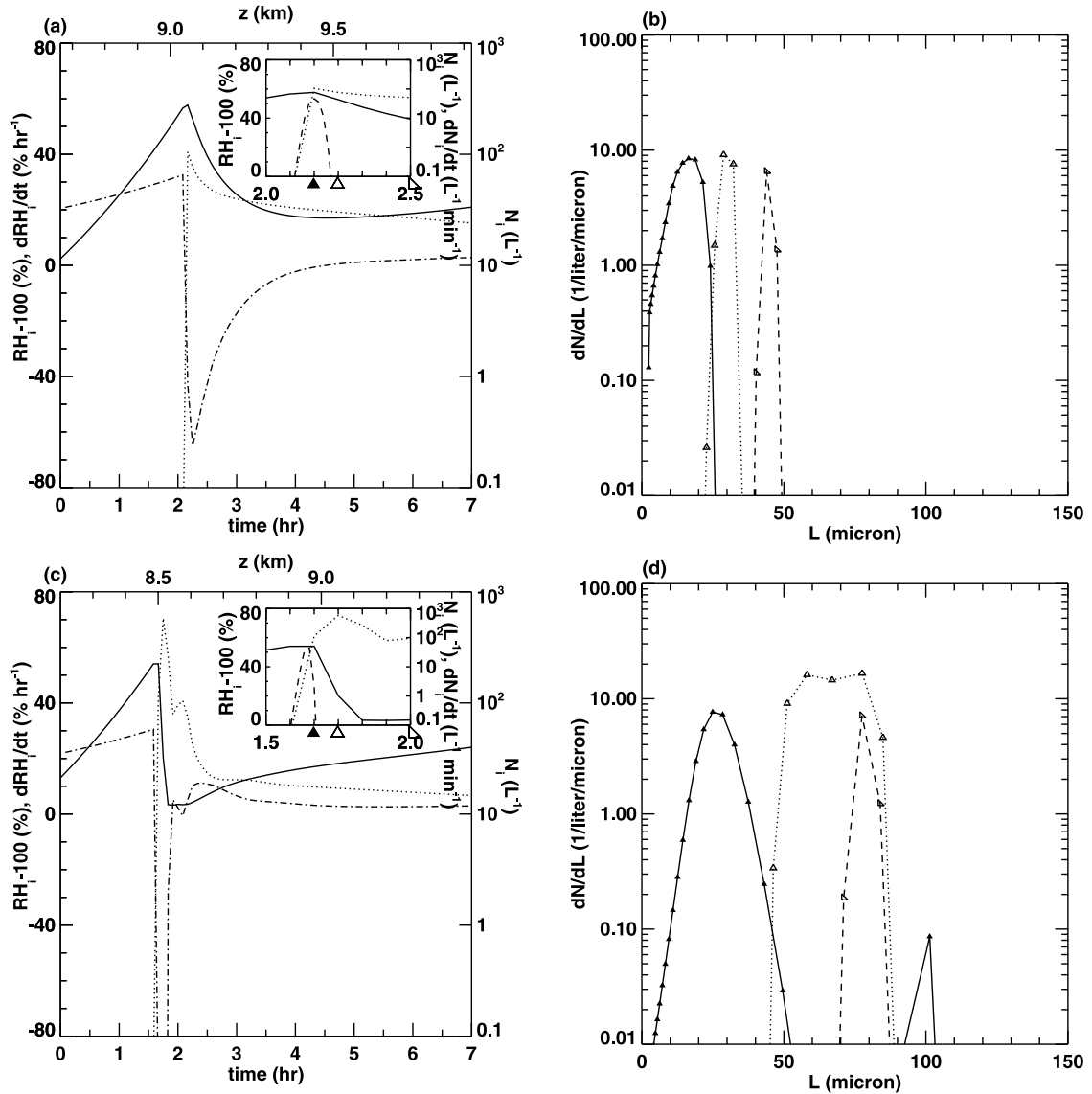
Figure 7. The evolution of trajectories (a and b) A and (c and d) B. RH_i-100 (solid), N_i (dotted), $\dot{N}_i$ (dashed), and dRH_i/dt (dash-dotted) are displayed in Figures 7a and 7c. Particle size distributions (PSDs) are displayed in Figures 7b and 7d, where corresponding time is indicated by the corresponding markers in the insets in Figures 7a and 7c.
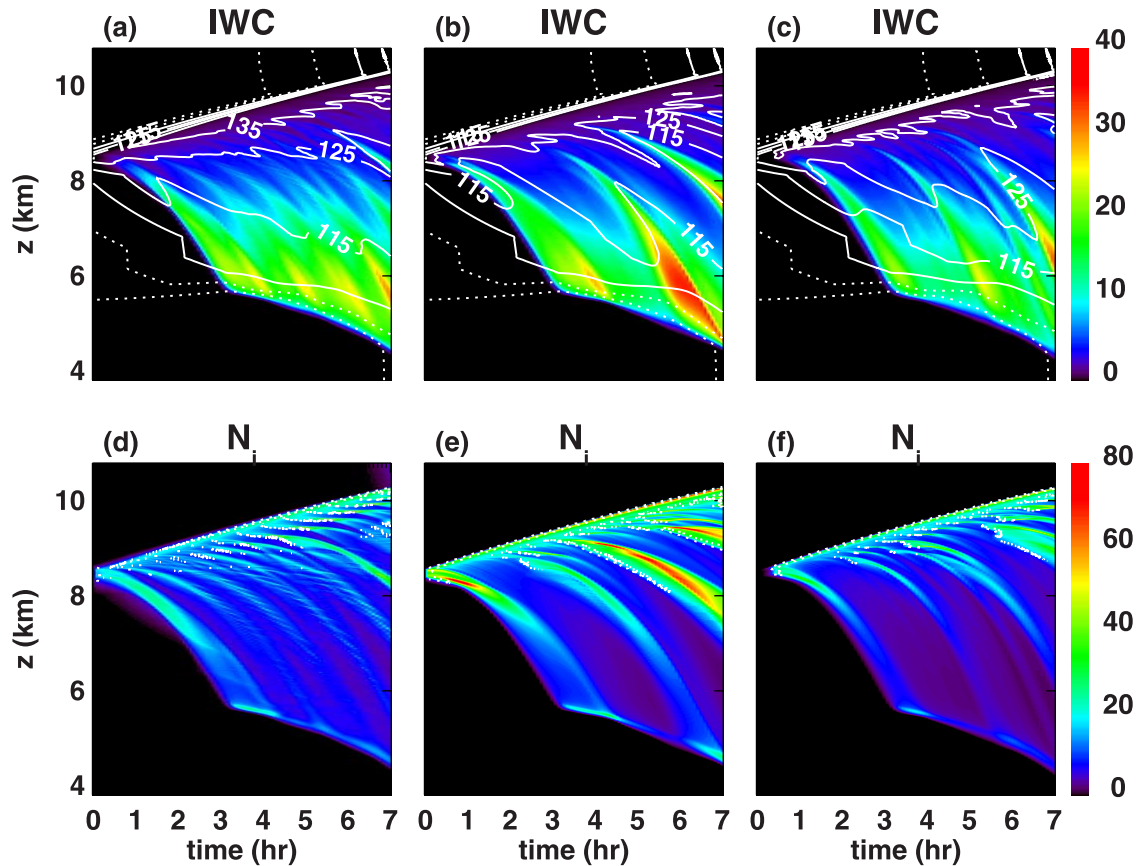
Figure 8. Similar to Figure 4, but effects of heterogeneous nucleation parameters on IWC (mg m^{-3}) and N_i (liter^{-1}). From left to right: M92, S20β60, and S30β60.

encounters the descending fall streak (Figure 4f). Similar to trajectory A, more than 100 L^{-1} of ice particles are present in trajectory B at the end of nucleation ($t = 100$ min, Figure 7c). The PSD indicates that at this time a small number of 100 μm-sized particles have entered the parcel from above (Figure 7d). N_i increases dramatically and PSD broadens between 100 and 105 min as the lower part of the fall streak descends through the parcel. RH$_i$ decreases to 102% at 110 min and remains close to saturation for 25 min until the fall streak passes. The PSD at time 120 min represents the PSD of the upper part of the fall streak. This PSD is narrower, but the mean size is larger, about 70 μm. Broad PSDs imply that the histories of existent particles are substantially different, i.e., different nucleation time and/or altitude, which is attributed to the 200-m depth of the initial nucleation. In the layer of large N_i, the outgoing particle flux (downward positive) from the bottom can be compensated by the influx from the top, in contrast to outgoing particle flux exceeding influx from the top near the cloud top nucleation zone. The RH$_i$ change rate becomes positive before the entire fall streak passes.

[25] The evolution of trajectories A and B clearly shows that within a few minutes of time, ice crystals generated in parcel may exit the parcel and be replaced by incoming ice crystals. The single air parcel study of cirrostratus forced by weak forcing is thus limited to the nucleation stage and cannot be extended to study the evolution of the cloud bulk properties or mass transport.

[26] In contrast to the cloud top region, the fall streak features greater IWC and N_i and lower ice supersaturation. These drastic differences between the two regions are caused by differences in the nucleation zone depth (several hundred meters for cloud initiation resulting in the main fall streak versus 10 m for the continuing cloud top nucleation zone), indicating that the depth of the nucleation zone is an important parameter in predicting cloud properties. In addition, we find that particle flux divergence constantly affects the local N_i, even in the nucleation zones. It is also evident that the relationship between N_i in the nucleation zone and N_i in the cloud ice mass bearing zone (lower fall streak) is not straightforward and is a topic worthy of further exploration. Thus a good estimate of the number of crystals generated in the nucleation regions must be accompanied by a good estimate of the aforementioned particle flux divergence effect, which depends on the depth of nucleation zone, to parameterize cirrostratus bulk properties in mesoscale or large-scale models.

5. Heterogeneous Nucleation (HET) Scenario

[27] We now examine the HET process via the simulations listed in Table 1. For the ranges of S_i^* and β studied here, the time series of IWP and N_iP (not shown) indicated that the 20-m setup is acceptable (<10% difference) for all except test S20β60. For consistency, all simulations presented here used a grid spacing of 4 m. Homogeneous
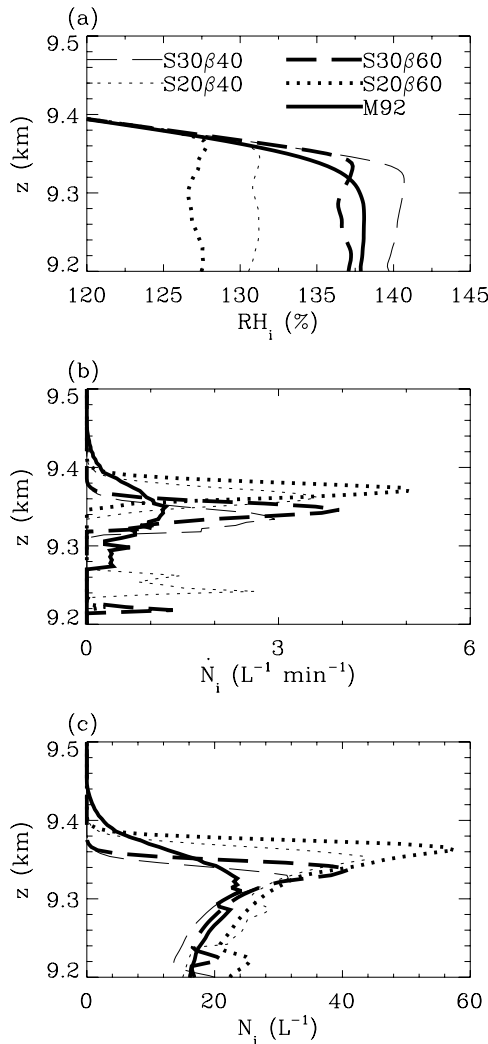
Figure 9. Effect of heterogeneous nucleation parameters on cloud-top nucleation zones at simulation time $t = 3$ hours. Note that the lower segments $\dot{N}_i$ of curves (z < 9.3 km) for cases S20β40 and S30β60 indicate midcloud nucleation.

nucleation is allowed but does not become active because the peak ice supersaturation never achieves sufficient magnitude. Aggregation is negligible because of the small N_i in these simulations.

[28] A prominent feature of the clouds in the HET runs is the periodic fall streaks (Figure 8). This contrasts with the occurrence of only one dominant fall streak in the 1-m HF simulation shown in Figures 4c and 4f. Layering of the consecutive fall streaks takes place. In addition to the response to the initial moist layer, two other nucleation zones emerge: the quasi-continuous cloud-top nucleation zone (small discontinuities due to IN bin discretization), as in the fine resolution HF runs, and an intermittent midcloud nucleation zone.

[29] The depth of the cloud-top nucleation zone and number of particles produced vary among the cases (Figure 9). Test M92 (smallest β) has the thickest cloud-top nucleation zone with a depth greater than 100 m, the depth is about 25–35 m in other HET tests, compared with 10 m in the HF run (largest effective β). This trend

indicates that the depth of cloud-top nucleation decreases with β. The peak S_i at the cloud top in Test M92 is much greater than the threshold S_i^*. With small β (Table 1), the particle formation rate is small and increases rather slowly as S_i increases beyond the activation S_i^*. When the particle formation rate is small, depositional growth of the relatively small quantity of ice crystals does not uptake much water vapor before they fall out, i.e., the few crystals grow rapidly. As S_i and the associated particle formation rate become large, the particle residence time and number concentration rise, i.e., more particles but smaller sizes. Ultimately, depositional growth of the newly activated particles is sufficient to drive dS_i/dt negative and eventually terminate further cloud top nucleation. For the rest of the HET simulations, for a given S_i^* within the cloud-top nucleation zone, an increase in β is associated with a greater peak particle formation rate but smaller peak RH_i. Given β, lowering the nucleation threshold S_i^* also results
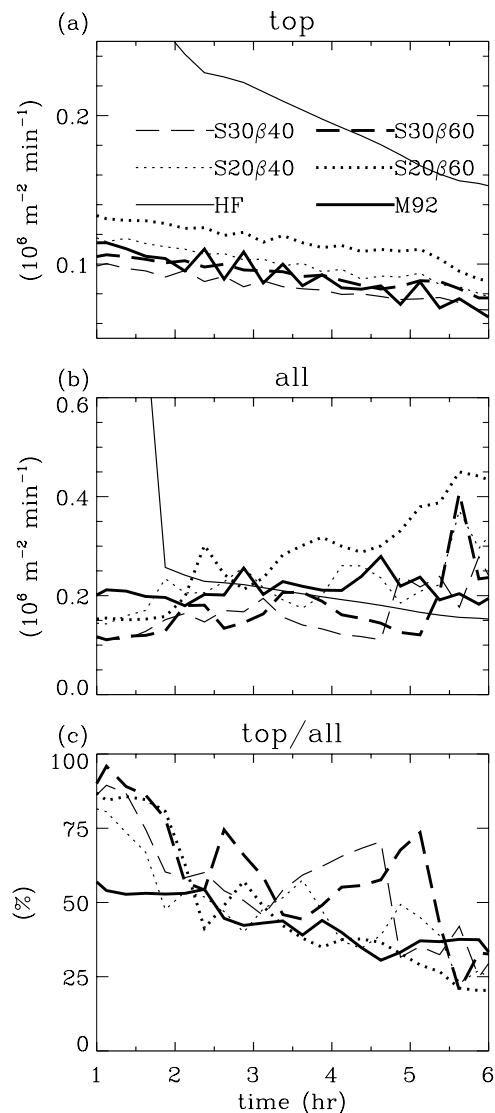
Figure 10. Column-integrated particle formation rates for (a) the cloud top nucleation zone and (b) for the entire air column. (c) The relative contribution of cloud-top nucleation in the HET cases.
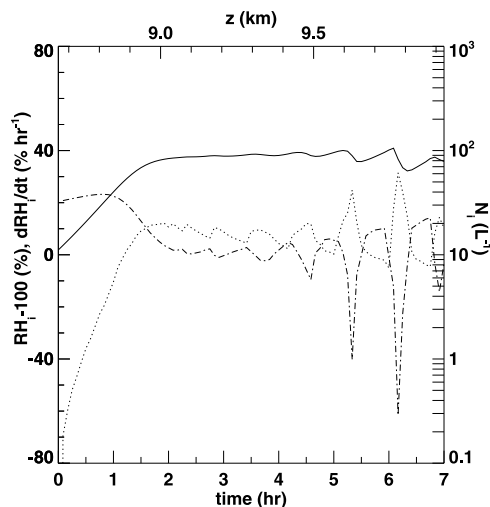
Figure 11. The evolution of a parcel trajectory released at $z_0 = 8.666$ km in Test M92, where RH_i-100 is indicated by the solid curve, N_i is denoted by the dotted curve, and dRH_i/dt is indicated by the dash-dotted curve.

in reduced peak RH_i but leads to an increased particle formation rate and a slight elevation of the nucleation zone. The effects of S_i^* and β are also reflected in the column-integrated particle formation rates in the cloud-top zone (Figure 10a), where the relative differences are maintained throughout the simulations.

[30] RH_i in the HET simulations does not decrease significantly below the cloud-top nucleation zone (Figure 9a). This indicates that the particle growth there is insufficient to uptake enough water vapor to limit the values of S_i. We see from the RH_i contours in Figure 8 that the upper part of the cloud remains highly supersaturated.

[31] Midcloud nucleation, which is activated when relative humidity is on the rise and IN are available, occurs and acts to limit S_i. The nucleation pulse mechanism, briefly discussed in the previous section, explains the formation of the midcloud nucleation zones. The premise of the midcloud growth-sedimentation-nucleation cycle is that the cloud-top nucleation zone does not produce a sufficient number of ice crystals that would sediment into the midcloud and limit RH_i via growth. Below the cloud-top nucleation zone, when particles coming from above cannot effectively uptake water vapor, S_i increases in response to continuous forcing (W). New ice crystals form when IN_k are available and their associated $S_{i,k+1}$ is achieved. The new ice crystals grow and fall out, and another cycle begins. Considering a trajectory that passes through the cloud top nucleation zone (the first 2.5 hours of the trajectory displayed in Figure 11) and then midcloud nucleation zones, the continuous forcing via W results in S_i achieving not only the corresponding nucleation threshold S_i^* (and initial crystal nucleation) but also, later, new successively larger peaks of S_i in the midcloud region (the trajectory after 2.5 hours in Figure 11) and thus renewed nucleation. In contrast, for the HF simulation with high S_i^* and β, the midcloud S_i does not achieve S_i^* and a midcloud generation zone never forms during the 7-hour simulation. Midcloud nucleation acts to broaden the PSDs, as illustrated

in Figure 12. The PSDs of the HET scenarios are much broader than those in the HF scenario (e.g., Figure 7). The PSDs can be segmented due to the intermittent nature of midcloud nucleation.

[32] We further define cloud-top nucleation as any nucleation taking place in air initially located in the layer above 8.2 km before its first peak S_i. For example, dRH_i/dt is positive initially and becomes zero at $t = 2.5$ hours in the trajectory shown in Figure 11. That is, the air along the trajectory is in the cloud-top nucleation zone in the first 2.5 hours. We apply this method to all the trajectories above 8.2 km and then establish the lower boundary of the cloud-top nucleation zone as a function of time for each simulation. The relative contributions of the cloud-top and midcloud nucleation for time period t = 1 to 6 hours (i.e., excluding the initial cloud formation event) are plotted in Figure 10. The column-integrated cloud-top contribution decreases with time in response to the decrease in the depth of the cloud-top nucleation zone, while its relative contribution, though oscillating, also decreases with time. The cumulative cloud-top contribution in the five HET cases (t = 2.5 to 6 hours) is less than 50% (Table 3), reflecting the importance of midcloud nucleation when there are sufficient IN such that HET is the dominant nucleation process. Ignoring midcloud nucleation will result in an overestimate of midcloud water vapor and an underestimate of cloud ice.

[33] The IWP, N_iP, and optical depth of all the simulations (4 m for all HET cases and 1 m for the HF case) are shown in Figure 13. Nucleation starts later in the HF simulation because more time is required for the forcing (W) to raise S_i to the required threshold, which is much larger than for HET. Thereafter, the HF simulation quickly produces the greater values of N_iP until t = 6 hours. The values of IWP and optical depth in HF also exceed those in the HET cases, but not until after 3 hours. This implies that if the large-scale forcing does not sustain for a long time, the HET scenario might be more efficient in producing ice and transporting water downward via particle sedimentation. The grouping of HET results (Figure 13) indicates that these bulk properties are more sensitive to S_i^* than β (for $0.2 \leq S_i^* \leq 0.3$ and $40 \leq \beta \leq 60$), although larger β does entail a slight increase of N_i and optical depth. The properties of the M92 simulation are close to the S20 cases, although significant differences exist in the morphology of the cloud (Figure 8).

[34] Figure 13 also shows that the trend of optical depth follows that of IWP but is further enhanced by differences in the bulk mass extinction coefficient, defined as optical depth divided by IWP, which depends on the effective particle size of the entire cloud layer. Furthermore, in this type of cirrus with high ice supersaturation and low ice particle count, an increase in N_iP entails more effective water vapor uptake and thus greater IWP. This suggests that one cannot treat the parameterization of IWP and cloud bulk effective radius as two separate issues for synoptically forced cirrostratus.

[35] For completeness, sensitivity tests are performed on alternative IN diagnostic schemes and on the relationship used to estimate ice crystal terminal velocities. In comparison to the IN tracking scheme we have used here, schemes may diagnose activation of IN by checking (1) $dS_i/dt > 0$ if
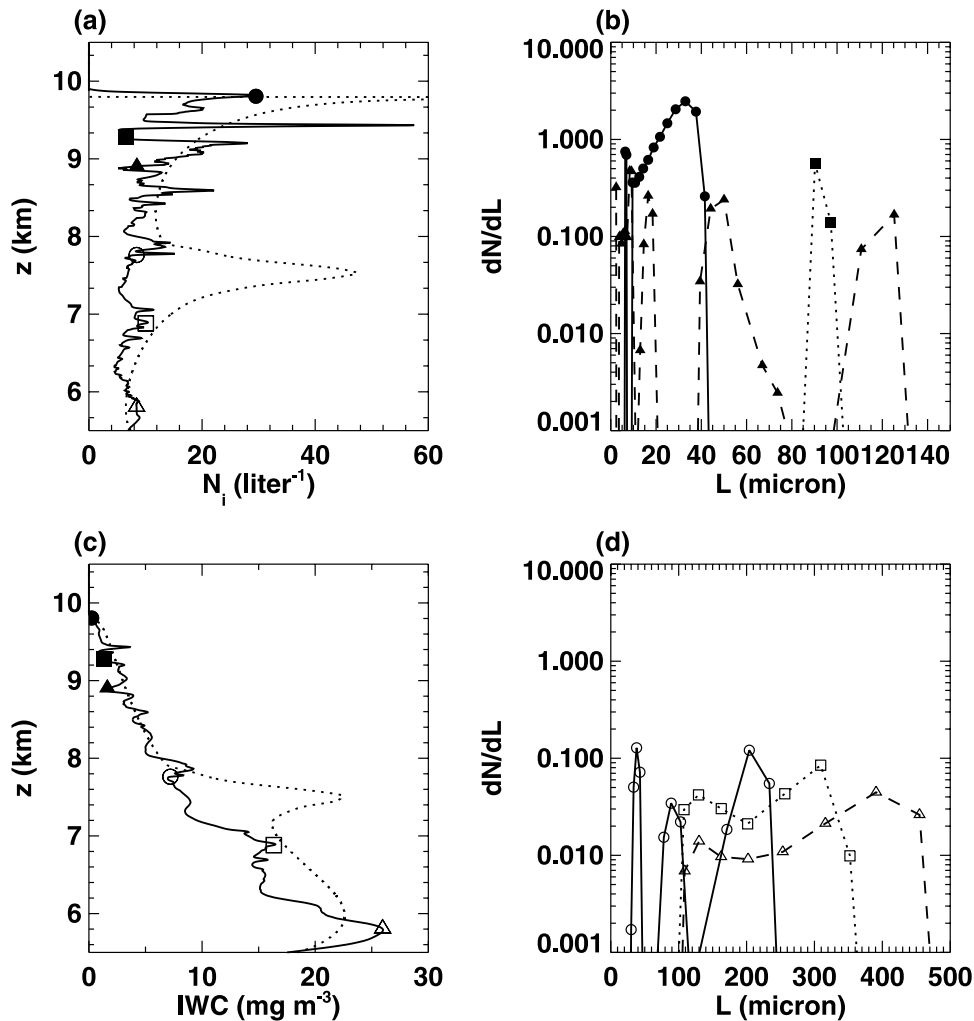
Figure 12. Left panels: N_i and IWC profiles of Test M92 (solid) and HF (dotted) at simulation time $t = 5$ hours. (right) PSDs (M92) at given heights, indicated by (left) the corresponding markers.

$S_i > 0$ (similar idea may be applied to formula based on temperature and height) and (2) Max ($N_{IN}(S_i) - N_i$, 0) if $S_i > 0$, respectively. The former (diagnose 1 in Figure 14) treats IN as if they are self-replenishing; the latter (diagnose 2 in Figure 14) treated IN as if they move with the ice particles, not with the air. Both diagnostic schemes overestimate N_iP (Figure 14). The former diagnostic scheme does a good job for the cloud-top nucleation zone but overestimates the midcloud nucleation and IWP. The latter diagnostic scheme overestimates cloud-top nucleation but underestimates the cloud-top RH_i as well as midcloud nucleation. However, the sensitivity is smaller compared to the sensitivity to β and S_i^* (Figure 14 vs. Figure 13). Therefore IN tracking is not a priority to simulate cirrostratus forced by a smooth and uniform ascent.

[36] Sensitivity to the specification of ice crystal terminal fall velocity is evaluated by either increasing or reducing the fall speed for each crystal size bin by 50% for the M92 and HF simulations. As expected, the cloud-top height is not much affected by the change of fall velocity of ice crystals. The evolution of the cloud-base height is affected by the change, especially in the first 3–4 hours where it is mainly controlled by the sedimentation of the first fall streak. At simulation time $t = 7$ hours, the maximum difference in cloud-base height among the sensitivity tests is about 1 km (±0.5 km). Reducing the fall velocity of ice crystals by 50% results in a rather dominate first fall streak, much more IWP and N_iP. Although the bulk microphysical properties are sensitive to the terminal fall velocity of ice crystals, the mechanisms that result in the development of the various nucleation zones are not altered.
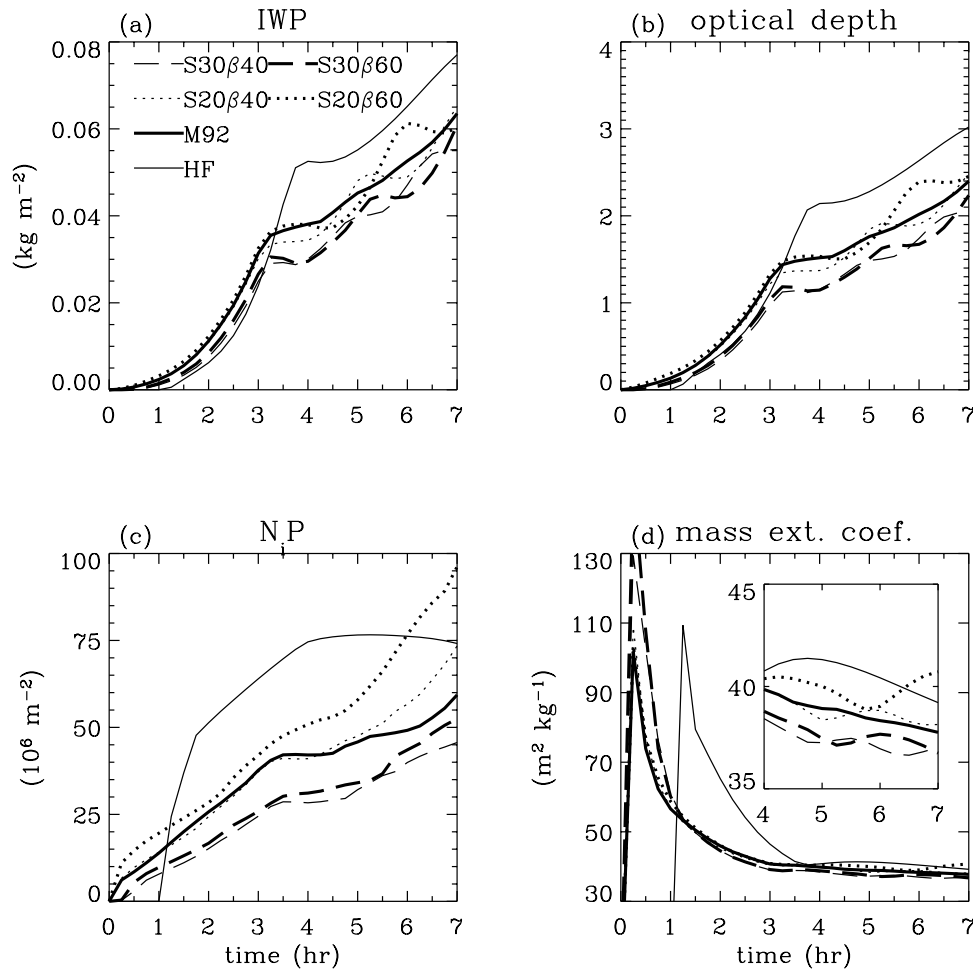
6. Conclusion

[37] A one-dimensional cirrus model with explicit microphysics is used to study the formation and evolution of

Table 3. Relative Contribution of the Cloud-Top Nucleation Between Simulation Times $t = 2.5$ and 6 Hours

| Run ID	Top/All
M92	38.7%
S20β60	34.4%
S20β40	40.0%
S30β60	48.2%
S30β40	45.7%

Figure 13. A comparison of the HF and HET bulk microphysical properties (IWP and N_iP) and optical properties at wavelength 0.55 μm (optical depth and mass extinction coefficient of the cloudy layer). Optical depths were calculated assuming ice particles of exclusively columnar hexagonal shape.

a cirrostratus forced by weak vertical motion. A series of tests on the nucleation modes (homogeneous-freezing-only versus heterogeneous nucleation) and heterogeneous nucleation parameters (β and S_i^*, defined in section 1) are performed. Owing to lack of in situ measurements of ice nuclei, we tested five pairs of β and S_i^*. The choice of the tested β and S_i^* is based on our assumption that these parameters are bounded by those estimated in the work of *Meyers et al.* [1992] and the effective β and S_i^* for the homogeneous freezing of haze particles. The choice of β is further guided by parcel simulations of the immersion freezing of haze particles. This study shows that when heterogeneous nucleation is the dominant nucleation process, the complex structure of cirrostratus may result solely from the episodic nature of nucleation, particle growth and sedimentation in the absence of turbulence and cloud-scale dynamical processes. In particular, in order to accurately predict the number of ice crystals and their size distribution within cirrus cloud layers, we find that the depth of nucleation zone, usually much, much smaller than the vertical grid spacing for the upper troposphere in GCMs and in cloud resolving models (CRMs), should be explicitly represented in parametric treatments of ice cloud generation.

[38] Other important findings are as follows:

[39] 1. Three types of nucleation regions exist in the cloud studied. First, the nucleation responds to the prescribed moist layer and occurs over a depth defined by the initial humidity structure. This would correspond to cloud initiation (formation). Second, in the presence of continuous adiabatic forcing, a continuous nucleation region occurs at cloud top and elevates with time with a speed greater than the imposed gentle updraft. This region is caused by haze particles or ice nuclei reaching freezing/nucleation threshold in the RH_i-decreasing-with-height layer that bounds the initially prescribed moist layer from above. Contribution of the cloud-top nucleation zone has been ignored by parcel simulation studies. Last, for the heterogeneous nucleation cases, intermittent nucleation occurs in midcloud regions in which ice crystals are formed when RH_i is on the rise and IN are available.

[40] 2. The depth of the cloud-top nucleation zone depends on β, given background thermodynamic variable profiles. For the HF only scenario (large effective β), the cloud-top nucleation zone is very thin and a model resolution as fine as 1 m is required to obtain a good approximation of the generated N_i. For the HET scenario, a resolution of 20 m may be required.
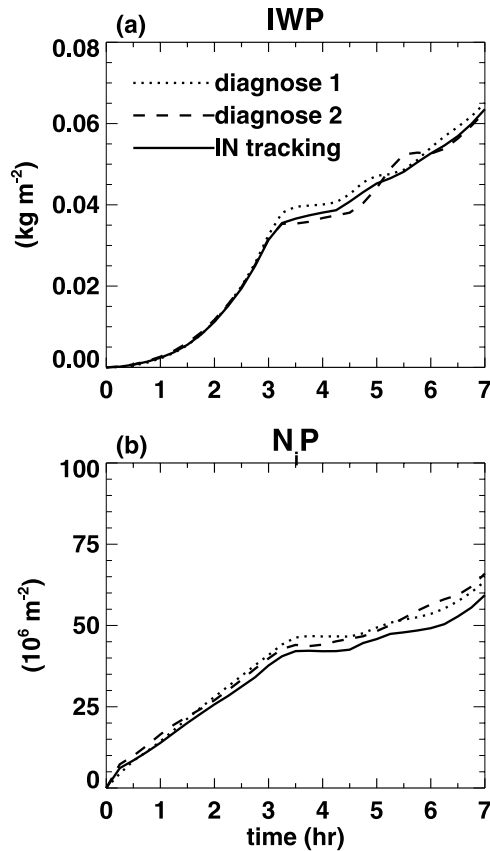
Figure 14. Effect of IN tracking/diagnosing schemes on IWP and N_iP.

[41] 3. Intermittent midcloud nucleation reduces water vapor and broadens the PSDs in the cloud. A combination of large S_i^* and extremely large β (the HF scenario) results in complete disappearance of the midcloud nucleation zone in this study. In contrast, small β and, especially, a small S_i^* entails a greater contribution by midcloud nucleation. The contribution of midcloud HET nucleation is more sensitive to S_i^* than to β for the ranges studied here and dominates the overall particle production by the cloud. Systematic differences in PSDs exist between the homogeneous-freezing-only (narrower PSDs) and heterogeneous nucleation (broader PSDs) scenarios in the studied case, owing to the midcloud nucleation and greater depth of nucleation zones in the heterogeneous nucleation scenario.

[42] 4. In all simulations, the mid-upper portion of the cloud is quite humid (RH > 120%) except within the initial fall streak in the HF scenario. With regard to in-cloud ice supersaturation, the cirrus studied here does not represent a rare case. High ice supersaturation has been frequently observed by the ARM Raman lidar at the Southern Great Plain (SGP) site [*Comstock et al.*, 2004] and also in subtropcial/tropical anvil and tropical cold thin cirrus [*Gao et al.*, 2004]. In the low ice particle count cirrostratus presented in this study, IWP and excess water vapor depend on ice particle path N_iP, i.e., more ice crystals enhance the uptake of water vapor and thus also the cloud IWP.

[43] The presented paper is a heuristic and theoretical exploration of the nucleation zones in cirrostratus based on

simple but reasonable assumptions. To gain a more quantitative assessment of given cases, we plan to adopt the single column model [e.g., *Randall et al.*, 1996; *Khvorostyanov et al.*, 2001] framework, in which the modeled column is driven by derived large-scale or mesoscale forcing data and the advection terms of moisture and heat (potential temperature) will be included.

Notation

C_k Capacitance for bin k.
C_p Specific heat of air at constant pressure.
D' Modified diffusivity of water vapor in air.
d Ice particle width.
e_i Saturation vapor pressure over plane ice surface.
g Acceleration of gravity.
K' Modified thermal conductivity.
L Ice particle length.
L_s Latent heat of sublimation.
m_k H_2O mass for bin k.
N_0 10^3 m^{-3}.
N_a Haze particle number concentration.
N_i Ice crystal number concentration.
$\dot{N}_i$ Ice particle formation rate.
N_{IN} Activated IN number concentration.
P Pressure.
q Water vapor mixing ratio.
q_s Saturation water vapor mixing ratio.
R_d Specific gas constant for dry air.
R_v Specific gas constant for water vapor.
RH_i Relative humidity with respect to ice.
S_i Ice supersaturation ratio.
S_i^* IN activation ice supersaturation ratio.
T Temperature.
T_{eff} Effective freezing temperature.
ΔT_m Melting point depression.
V_t Terminal fall speed.
W Synoptic scale vertical wind.
Δz Vertical grid spacing.
β IN parameterization coefficient.
ε 0.622.
ρ Air density.
$(\ )_k$ Bin number.

References

Allen, D. J., A. R. Douglass, R. B. Rood, and P. D. Guthrie (1991), Application of a monotonic upstream-biased transport scheme to three-dimensional constituent transport calculations, *Mon. Weather Rev.*, 119, 2456–2464.

Auer, A. H., Jr., and D. L. Veal (1970), The dimension of ice crystals in natural clouds, *J. Atmos. Sci.*, 27, 919–926.

Bailey, M., and J. Hallett (2004), Growth rates and habits of ice crystals between −20° and −70°, *J. Atmos. Sci.*, 61, 514–544.

Böhm, H. P. (1989), A general equation for the terminal fall speed of solid hydrometeors, *J. Atmos. Sci.*, 46, 2419–2427.

Chen, J.-P., and D. Lamb (1994), Simulations of cloud microphysical and chemical processes using a multicomponent framework. Part I: Description of the microphysical model, *J. Atmos. Sci.*, 51, 3505–3516.

Comstock, J. M., T. P. Ackerman, and D. D. Turner (2004), Evidence of high ice supersaturation in cirrus clouds using ARM Raman lidar measurements, *Geophys. Res. Lett.*, 31, L11106, doi:10.1029/2004GL019705.

Del Genio, A. D., M.-S. Yao, W. Kovari, and K. K.-W. Lo (1996), A prognostic cloud water parameterization for global climate models, *J. Climate*, *9*, 270–304.

DeMott, P. J., D. C. Rogers, and S. M. Kreidenweis (1997), The susceptibility of ice formation in upper tropospheric clouds to insoluble aerosol components, *J. Geophys. Res.*, *102*, 19,575–19,584.

Foot, J. S. (1988), Some observations of the optical properties of clouds, II: Cirrus, *Q. J. R. Meteorol. Soc.*, *114*, 145–164.

Fowler, L. D., D. A. Randall, and S. A. Rutledge (1996), Liquid and ice cloud microphysics in the CSU General Circulation Model. Part I: Model description and simulated microphysical processes, *J. Climate*, *9*, 489–529.

Gao, R. S., et al. (2004), Evidence that nitric acid increases relative humidity in low-temperature cirrus clouds, *Science*, *303*, 516–520.

Gierens, K. M., M. Monier, and J.-F. Gayet (2003), The deposition coefficient and its role for cirrus clouds, *J. Geophys. Res.*, *108*(D2), 4069, doi:10.1029/2001JD001558.

Haag, W., B. Kärcher, S. Schaefers, O. Stetzer, O. Möhler, U. Schurath, M. Krämer, and C. Schiller (2003a), Numerical simulations of homogeneous freezing processes in the aerosol chamber AIDA, *Atmos. Chem. Phys.*, *3*, 195–210.

Haag, W., B. Kärcher, J. Ström, A. Minikin, U. Lohmann, J. Ovarlez, and A. Stohl (2003b), Freezing thresholds and cirrus cloud formation mechanisms inferred from in situ measurements of relative humidity, *Atmos. Chem. Phys.*, *3*, 1791–1806.

Haynes, D. R., N. J. Tro, and S. M. George (1992), Condensation and evaporation of H_2O on ice surfaces, *J. Phys. Chem.*, *96*, 8502–8509.

Heymsfield, A. J. (1972), Ice crystal terminal velocity, *J. Atmos. Sci.*, *29*, 1348–1357.

Heymsfield, A. J., and L. M. Miloshevich (1993), Homogeneous ice nucleation and supercooled liquid water in orographic wave clouds, *J. Atmos. Sci.*, *50*, 2335–2353.

Heymsfield, A. J., and L. M. Miloshevich (1995), Relative humidity and temperature influences on cirrus formation and evolution: Observations from wave clouds and FIRE II, *J. Atmos. Sci.*, *52*, 4302–4326.

Heymsfield, A. J., and L. M. Miloshevich (1998), The dependence of cirrus ice crystal growth rates on temperature: Theory versus in-situ observations, paper presented at Conference on Cloud Physics and 14th Conference on Planned and Inadvertent Weather Modification, Am Meteorol. Soc., Everett, Wash.

Jensen, E. J., O. B. Toon, D. L. Westphal, S. Kinne, and A. J. Heymsfield (1994a), Microphysical modeling of cirrus: 1. Comparison with 1986 FIRE IFO measurements, *J. Geophys. Res.*, *99*, 10,421–10,442.

Jensen, E. J., O. B. Toon, D. L. Westphal, S. Kinne, and A. J. Heymsfield (1994b), Microphysical modeling of cirrus: 2. Microphysical modeling of cirrus, *J. Geophys. Res.*, *99*, 10,443–10,454.

Kärcher, B., and U. Lohmann (2002), A parameterization of cirrus cloud formation: Homogeneous freezing of supercooled aerosols, *J. Geophys. Res.*, *107*(D2), 4010, doi:10.1029/2001JD000470.

Khain, A., M. Ovtchinnikov, M. Pinsky, A. Pokrovsky, and H. Krugliak (2000), Notes on the state-of-the-art numerical modeling of cloud microphysics, *Atmos. Res.*, *55*, 159–224.

Khvorostyanov, V. I., and K. Sassen (1998), Cirrus cloud simulation using explicit microphysics and radiation. Part I: Model description, *J. Atmos. Sci.*, *55*, 1808–1821.

Khvorostyanov, V. I., J. A. Curry, J. O. Pinto, M. Shupe, B. A. Baker, and K. Sassen (2001), Modeling with explicit spectral water and ice microphysics of a two-layer cloud system of illustrated and cirrus observed during the FIRE Arctic Clouds Experiment, *J. Geophys. Res.*, *106*, 15,099–15,112.

Koop, T., B. Luo, A. Tsias, and T. Peter (2000), Water activity as the determinant for homogeneous ice nucleation in aqueous solutions, *Nature*, *406*, 611–614.

Lin, R.-F. (1997), A numerical study of the evolution of nocturnal cirrus by a two-dimensional model with explicit microphysics, Ph.D. thesis, 199 pp., Penn. State Univ., University Park, Penn.

Lin, R.-F., D. O. Starr, P. J. DeMott, R. Cotton, K. Sassen, E. Jensen, B. Kärcher, and X. Liu (2002a), Cirrus parcel model comparison project phase 1. The critical components to simulate cirrus initiation explicitly, *J. Atmos. Sci.*, *59*, 2305–2329.

Lin, R.-F., D. O. Starr, P. J. DeMott, R. Cotton, E. Jensen, B. Kärcher, and X. Liu (2002b), Cirrus parcel model comparison project phase 2, paper presented at 11th Conference on Cloud Physics, Am. Meteorol. Soc., Ogden, Utah, 3–7 June.

Lohmann, U., and B. Kärcher (2002), First interactive simulations of cirrus clouds formed by homogeneous freezing in the ECHAM general circulation model, *J. Geophys. Res.*, *107*(D10), 4105, doi:10.1029/2001JD000767.

Meyers, P. J., P. J. DeMott, and W. R. Cotton (1992), New primary ice-nucleation parameterizations in an explicit cloud model, *J. Appl. Meteorol.*, *31*, 708–721.

Mitchell, D. L., and W. P. Arnott (1994), A model predicting the evolution of ice particle size spectra and radiative properties of cirrus clouds. Part II: Dependence of absorption and extinction on ice crystal morphology, *J. Atmos. Sci.*, *51*, 817–832.

Ochs, H. T., III, and C. S. Yao (1978), Moment-conserving techniques for warm cloud microphysical computations. Part I. Numerical techniques, *J. Atmos. Sci.*, *35*, 1947–1958.

Pruppacher, H. R., and J. D. Klett (1997), *Microphysics of Clouds and Precipitation*, 2nd ed., 954 pp., Springer, New York.

Randall, D. A., K.-M. Xu, R. J. C. Somerville, and S. Iacobellis (1996), Single-column models and cloud ensemble models as links between observations and climate models, *J. Climate*, *9*, 1683–1697.

Reichardt, J., U. Wandinger, M. Serwazi, and C. Weitkamp (1996), Combined Raman lidar for aerosol, ozone, and moisture measurements, *Opt. Eng.*, *35*, 1457–1465.

Reichardt, J., S. Reichardt, A. Behrendt, and T. J. McGee (2002a), Correlations among the optical properties of cirrus-cloud particles: Implications for spaceborne remote sensing, *Geophys. Res. Lett.*, *29*(14), 1668, doi:10.1029/2002GL014836.

Reichardt, J., R.-F. Lin, S. Reichardt, T. J. McGee, and D. O. Starr (2002b), Microphysical interpretation of cirrus measurements with lidar- Comparison to a coupled optical-microphysical model, paper presented at 11th Conference on Atmospheric Radiation, Am. Meteorol. Soc., Ogden, Utah.

Rokicki, M. L., and K. C. Young (1978), The initiation of precipitation in updrafts, *J. Atmos. Sci.*, *17*, 745–754.

Sassen, K., and G. C. Dodd (1988), Homogeneous nucleation rate for highly supercooled cirrus cloud droplets, *J. Atmos. Sci.*, *45*, 1357–1369.

Sassen, K., D. O. Starr, and T. Uttal (1989), Mesoscale and microscale structure of cirrus clouds: Three case studies, *J. Atmos. Sci.*, *46*, 371–396.

Sassen, K., C. J. Grund, J. D. Spinhirne, M. Hardesty, and J. M. Alvarez (1990), The 27–28 October 1986 FIRE IFO cirrus case study: A five lidar overview of cloud structure and evolution, *Mon. Weather Rev.*, *118*, 2288–2311.

Sassen, K., Z. Wang, V. I. Khvorostyanov, G. L. Stephens, and A. Bennedetti (2002), Cirrus cloud ice water content radar algorithm evaluation using an explicit cloud microphysical model, *J. Appl. Meteorol.*, *41*, 620–628.

Starr, D. O., and D. P. Wylie (1990), The 27–28 October 1986 FIRE cirrus case study: Meteorology and clouds, *Mon. Weather Rev.*, *118*, 2259–2287.

Stephens, G. L. (1983), The influence of radiative transfer on the mass and heat budgets of ice crystals falling in the atmosphere, *J. Atmos. Sci.*, *40*, 1729–1739.

Tzivion, S., G. Feingold, and Z. Levin (1987), An efficient numerical solution to the stochastic collection equation, *J. Atmos. Sci.*, *44*, 3139–3149.

———————————

P. J. DeMott, Department of Atmospheric Science, Colorado State University, Fort Collins, CO 80523, USA.

R.-F. Lin, Goddard Earth Sciences and Technology Center, University of Maryland Baltimore County, Code 613.1, Greenbelt, MD 20771, USA. (lin@agnes.gsfc.nasa.gov)

J. Reichardt, DWD-Meteorologisches Observatorium Lindenberg, D-15848 Tauche, Germany.

D. O. Starr, Laboratory for Atmospheres, NASA Goddard Space Flight Center, Code 613.1, Greenbelt, MD 20771, USA.